

# Constraining SIDM with halo shapes: revisited predictions from realistic simulations of early-type galaxies

Giulia Despali<sup>1\*</sup>, Levi G. Walls<sup>2,3</sup>, Simona Vegetti<sup>3</sup>, Martin Sparre<sup>4,5</sup>, Mark Vogelsberger<sup>6</sup>, Jesús Zavala<sup>7</sup>

<sup>1</sup> Institut für Theoretische Astrophysik, Zentrum für Astronomie, Heidelberg Universität, Albert-Ueberle-Str. 2, 69120, Heidelberg, Germany

<sup>2</sup> Department of Astronomy, University of Michigan, 323 West Hall, 1085 S. University, Ann Arbor, MI 48109 USA

<sup>3</sup> Max Planck Institute for Astrophysics, Karl-Schwarzschild-Strasse 1, 85748 Garching bei München, Germany

<sup>4</sup> Institut für Physik und Astronomie, Universität Potsdam, Karl-Liebknecht-Str. 24/25, D-14476 Golm, Germany

<sup>5</sup> Leibniz-Institut für Astrophysik Potsdam (AIP), An der Sternwarte 16, 14482 Potsdam, Germany

<sup>6</sup> Department of Physics, Kavli Institute for Astrophysics and Space Research, Massachusetts Institute of Technology, Cambridge, MA 02139, USA

<sup>7</sup> Center for Astrophysics and Cosmology, Science Institute, University of Iceland, Dunhagi 5, 107 Reykjavík, Iceland

Submitted to MNRAS, April 2022

## ABSTRACT

We study the effect of self-interacting dark matter (SIDM) and baryons on the shapes of early-type galaxies (ETGs) and their dark matter haloes, comparing them to the predictions of the standard cold dark matter (CDM) scenario. We use a sample of five zoom-in simulations of haloes hosting ETGs ( $M_{\text{vir}} \sim 10^{13} M_{\odot}$  and  $M_{*} \sim 10^{11} M_{\odot}$ ), simulated in CDM and a SIDM model with constant cross-section of  $\sigma_T/m_{\chi} = 1 \text{ cm}^2 \text{ g}^{-1}$ , with and without the inclusion of baryonic physics. We measure the three-dimensional and projected shapes of the dark matter haloes and their baryonic content by means of the inertia tensor and compare our measurements to the results of gravitational lensing and X-ray observations. We find that the inclusion of baryons greatly reduces the differences between CDM and a SIDM and thus the ability to draw constraints on the basis of shapes. We find that lensing measurements clearly reject the predictions from CDM dark-matter-only simulations, whereas they show a different degree of preference for the CDM and SIDM hydro scenarios, and cannot discard the SIDM dark-matter-only case. The shapes of the X-ray emitting gas are also comparable to observational results in both hydro runs, with CDM predicting higher elongations only in the very center. Contrary to previous claims at the scale of elliptical galaxies, we conclude that both CDM and our SIDM model with  $\sigma_T/m_{\chi} = 1 \text{ cm}^2 \text{ g}^{-1}$  are able to explain observed distributions of halo shapes, once baryons are included in the simulations.

**Key words:** cosmology: dark matter - methods: numerical - galaxies: halos - galaxies: elliptical and lenticular, cD - X-rays: galaxies - gravitational lensing: strong

## 1 INTRODUCTION

The foundations on which our current understanding of structure formation is based on is the  $\Lambda$ CDM model, which describes the Universe as filled with cold dark matter (CDM) that is collisionless and interacts only via the gravitational force. The CDM paradigm is widely successful in explaining many aspects of galaxy formation and evolution (Springel et al. 2005; Schaye et al. 2015; Vogelsberger et al. 2014a; Pillepich et al. 2018; Vogelsberger et al. 2020). However, the corresponding particles (e.g. WIMPs) required by the CDM model have not yet been found with direct nor indirect detection experiments (Roszkowski et al. 2018): other models have been proposed as possible alternatives to CDM, justified also by the well-known tensions between  $\Lambda$ CDM predictions and observations on cosmological (Verde et al. 2019) or small (Bullock & Boylan-Kolchin 2017) scales.

Among alternative models, self-interacting dark matter (SIDM)

postulates that dark matter particles are not collisionless, but can have strong interactions and exchange energy and momentum. SIDM was originally invoked to address the discrepancies between the observed properties of dwarf galaxies and the predictions from (DM-only) CDM simulations and has the potential to solve many of the small-scale CDM problems (for a review see Tulin & Yu 2018). The term SIDM refers to a variety of models that can include elastic or inelastic scattering, a constant or velocity-dependent interaction cross-section (Vogelsberger et al. 2012, 2016, 2019; Despali et al. 2019; Sameie et al. 2018, 2020; Rocha et al. 2013; Robertson et al. 2018, 2021; Lovell et al. 2019; Kaplinghat et al. 2014, 2019, 2020).

The most important signature of SIDM across all models is the creation of a central core in the density profile of haloes, due to the momentum and energy exchanges between the particles, with an extent that depends on the self-interaction cross-section (Colin et al. 2002; Rocha et al. 2013; Vogelsberger et al. 2012, 2014b, 2016). This process is efficient in the center of haloes where the density is high and leads to modifications of the central density cusp

\* E-mail: gdespali@uni-heidelberg.de

predicted by the standard NFW profile (Navarro et al. 1997). In the outskirts, where the density drops, the effects are negligible and the density profile tends to the NFW prediction. However, this simple picture is modified once the effect of baryons is considered: baryonic matter dominates the central region of haloes and, as demonstrated by CDM hydrodynamical simulations, can significantly alter the halo properties predicted by dark-matter only simulations. In CDM, the gradual growth of the baryonic potential has the effect of adiabatically contracting the dark matter halo and increasing its concentration (Blumenthal et al. 1986; Gnedin et al. 2004; Schaller et al. 2015; Lovell et al. 2019), while rapid events such as feedback and supernova explosions can lower the central density (Mashchenko et al. 2006; Pontzen & Governato 2012; Burger & Zavala 2021; Read et al. 2016; Tollet et al. 2016; Oñorbe et al. 2015). The inclusion of baryons can also alleviate some of the tensions between CDM and observations, such as the classic missing satellites and too-big-to-fail problems (Zolotov et al. 2012; Kim et al. 2018; Garrison-Kimmel et al. 2019) and create cored profiles (Benítez-Llambay et al. 2019). However, alternative dark matter models remain an active field, due to the difficulties of reproducing all observed properties with the same model and the lack of a definitive particle detection. In SIDM, the role of the dark matter and baryonic potentials depend on the self-interaction cross-section and on the timescales of SIDM interactions with respect to the time evolution of the dark matter density profile. Recent works have started to explore the interplay between SIDM and baryons, using hydrodynamical simulations at galaxy (Sameie et al. 2018; Despali et al. 2019) and galaxy cluster (Robertson et al. 2018, 2021; Shen et al. 2022) scales. The inclusion of baryons generally reduces the differences between CDM and SIDM predictions, with respect to dark-matter-only simulations: the baryonic potential of the central galaxy partially counteracts the flattening due to self-interactions.

In this work, we focus on another halo property that is affected by self-interactions: halo shape. In dark-matter-only simulations, the self-interactions between particles produce rounder central shapes than in the CDM scenario (Davé et al. 2001; Peter et al. 2013; Brinckmann et al. 2018). Previous works have used gravitational lensing (Miralda-Escudé 2002) and X-ray (Buote et al. 2002; McDaniel et al. 2021) observations to estimate the ellipticity (or triaxiality) of elliptical galaxies or clusters and set some of the strongest constraints on the allowed range of self-interaction cross-sections. Other recent works focus instead of similar constraints, but at the scale of galaxy clusters (Robertson et al. 2018; Shen et al. 2022; Andrade et al. 2022). The advantage of considering elliptical galaxies is twofold: early-type galaxies are common lens galaxies at high-redshift (Auger et al. 2010) and are well described by a smooth mass distribution (Enzi et al. 2020); moreover, in relaxed elliptical galaxies, it is reasonable to assume that the X-ray emitting interstellar gas is in hydrostatic equilibrium with the halo potential. Under this condition, the shape of the X-ray emission can be used to derive the overall shape of the dark matter halo. Applying this method to the elliptical galaxy NGC 720, Buote et al. (2002) determined a halo ellipticity of  $\epsilon \approx 0.35\text{--}0.4$  from Chandra X-ray data. A comparison to theoretical predictions for NFW and Hernquist profiles led to the conclusion that this value was consistent with an interaction cross-section of  $\sigma_T/m_\chi \sim 0.1\text{ cm}^2/\text{g}$  as well as with CDM, while higher self-interaction cross-section were disfavoured. A similar conclusion was reached by Peter et al. (2013), who compared these observational data to dark-matter-only simulations in CDM and SIDM. More recently, McDaniel et al. (2021) analysed Chandra and XMM-Newton observations of a sample of eleven elliptical galaxies and compared their X-ray surface brightness profile to the predicted emission generated by dark matter

haloes with varying density profile and triaxiality. Their findings led to milder constraints with respect to previous studies and showed that a self-interaction at the scale of  $\sigma_T/m_\chi \sim 1\text{ cm}^2/\text{g}$  would still be consistent with their observations (as well as the CDM scenario).

One important limitation of most previous works at the scale of massive galaxies is that the simulations used for the comparison with observational data did not include baryonic physics. It is well known that the inclusion of baryons can significantly alter the central shapes of CDM haloes (Chua et al. 2019), leading to rounder configurations with respect to CDM dark-matter-only runs. In practice, baryons and SIDM both affect halo shapes in a similar manner and thus their combination can alter the distribution of predicted shapes (Chua et al. 2021) and, as a consequence, to different constraints. The aim of this work is to improve the computational predictions at the scale of elliptical galaxies ( $M_{\text{vir}} \sim 10^{13} M_\odot$  and  $M_* \sim 10^{11} M_\odot$ ), by analysing the hydrodynamical zoom-in simulations from Despali et al. (2019) to determine the impact of the inclusion of baryonic physics on the dark matter halo shapes, in CDM and in a SIDM model with a cross-section of  $\sigma_T/m_\chi = 1\text{ cm}^2/\text{g}$ . These are the first simulations of early-type galaxies that include both baryonic physics (following the TNG model, see Pillepich et al. 2018) and self-interacting dark matter. We measure the intrinsic and projected shapes from the mass distribution, as well as the ellipticity of the simulated X-ray emission with mocks that reproduce Chandra and XMM-Newton data. We compare our findings with the shapes measured in previous works using gravitational lensing (Auger et al. 2010; Sonnenfeld et al. 2013; Ritondale et al. 2019) and X-ray data (Buote et al. 2002; McDaniel et al. 2021). In this respect, our work is similar to the recent analysis by Shen et al. (2022), who used SIDM simulations with similar cross-section and including adiabatic gas to compare the shape of the X-ray emission to observations of galaxy clusters.

The paper is organised as follows. In Section 2 we describe the simulations and Section 3 sets out our analysis process. In Section 4 we present the measurements of three-dimensional and projected shapes from the simulations, and compare them with observational data, while in Section 5 we analyse the X-ray mock images and compare them to real observations by Chandra and XMM-Newton. Finally, we discuss our results and draw our conclusions in Section 6. In the Appendix, we discuss technical aspects in more details.

## 2 SIMULATIONS

We use the sample of simulated galaxies from Despali et al. (2019). These are zoom-in re-simulations of systems chosen from the Illustris simulations (Vogelsberger et al. 2014a; Torrey et al. 2014; Genel et al. 2014) on the basis of their properties (Despali & Vegetti 2017), to resemble the lens galaxies from the SLACS survey (Bolton et al. 2006): haloes that host early-type galaxies (ETGs) at  $z \approx 0.2$  with total mass, stellar mass, stellar effective radius and velocity dispersion consistent with those of SLACS lenses. Among this population, Despali et al. (2019) have re-simulated a subsample of nine galaxies with the zoom simulation method described in Sparre & Springel (2016): the dark matter mass resolution is  $4.4 \times 10^6 M_\odot$ , while the baryonic resolution is  $9.1 \times 10^5 M_\odot$ . Each galaxy was re-simulated both in the standard CDM scenario and in a SIDM model with a constant cross-section of  $\sigma_T/m_\chi = 1\text{ cm}^2\text{g}^{-1}$ , using an extended version of the AREPO code that includes both elastic and multi-state inelastic SIDM (Vogelsberger et al. 2012, 2016, 2018). The IllustrisTNG physics model (Pillepich et al. 2018) was used to describe the evolution of baryonic physics, including AGN feedback (Weinberger et al. 2017) and magnetohydrodynamics (Pakmor & Springel 2013; Sparre

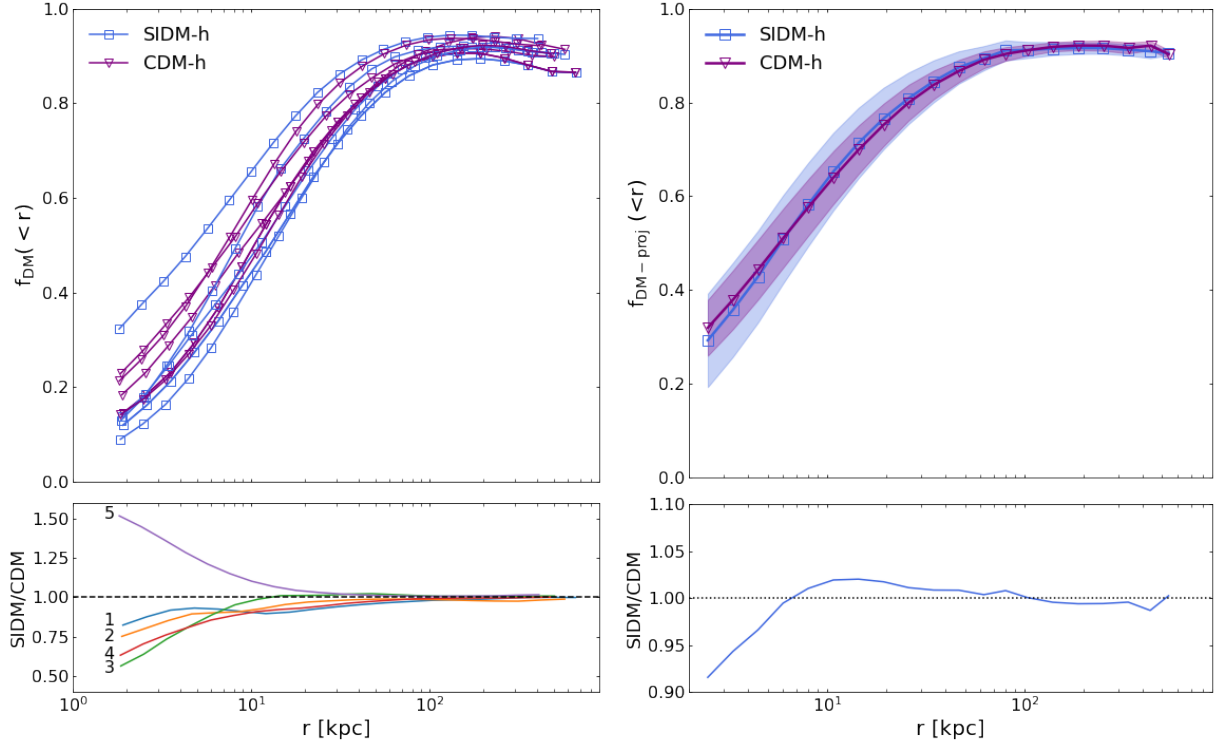


**Figure 1.** Fraction in dark matter as a function of radius in the CDM-h (purple, triangles) and SIDM-h (blue, squares) runs that include baryons, calculated in logarithmically spaced bins in the range  $[0.01, 1] \times R_{\text{vir}}$ . The left panel shows the dark matter fraction for each halo in both scenarios, whereas the right panel shows the average projected fraction over 90 viewing angles for each halo, together with the standard deviation. In the bottom panels, we show the ratio between the SIDM-h and CDM-h cases.

**Table 1.** Summary of halo properties in the CDM and SIDM runs: SUBFIND IDs in the parent Illustris simulations, total halo mass  $M_{\text{vir}}$ , stellar mass of the central galaxy  $M_*$  for the two hydro runs and virial radius expressed in *comoving* kpc. We refer the reader to [Despali et al. \(2019\)](#) for more details on each system. throughout the paper, CDM-d and SIDM-d are the dark-matter-only runs, while CDM-h and SIDM-h their counterparts including baryonic physics.

halo ID	$M_{\text{vir}} [10^{13} M_{\odot}]$				$R_{\text{vir}} [\text{kpc}]$				$M_* [10^{11} M_{\odot}]$	
	CDM-d	SIDM-d	CDM-h	SIDM-h	CDM-d	SIDM-d	CDM-h	SIDM-h	CDM-h	SIDM-h
1	2.66	2.67	3.73	3.76	940	941	937	938	4.08	4.50
2	2.13	1.81	2.45	2.46	872	835	815	813	2.71	3.02
3	1.24	1.24	1.64	1.65	730	728	714	713	2.16	1.75
4	1.10	1.10	1.4	1.41	698	700	678	676	3.03	3.04
5	0.71	0.74	0.91	0.86	605	613	585	572	1.46	1.42

[et al. 2020](#)). We point out that we have not re-calibrated the model in the case of SIDM. For this work, we also ran the SIDM dark-matter-only version of the each simulation, while we use the original dark-matter-only version from the Illustris1-Dark simulation as the CDM counterpart. In this case, the dark matter mass resolution is  $7 \times 10^6 M_{\odot}$ .

For simplicity, throughout the text we refer to the dark-matter-only simulations as CDM-d and SIDM-d, while to their counterparts that include baryonic physics as CDM-h and SIDM-h.

Some of the galaxies that were identified as ETGs in the original Illustris-1 run develop disks in our zoom-in simulations, due to the interplay between SIDM and baryons and the differences between the Illustris and the IllustrisTNG model (see [Despali et al. 2019](#), for more details). In this work, we focus on five galaxies which maintain ETG-like morphologies in both scenarios for an effective comparison with observational results based on ellipticals and ETGs. Haloes and subhaloes have been identified with the Friends-of-friends (FoF) method by SUBFIND ([Springel et al. 2005](#)) and a list of the main halo

and galaxy properties can be found in Table 1. We define the virial mass  $M_{\text{vir}}$  as the mass within the virial radius  $R_{\text{vir}}$  that encloses a virial overdensity  $\Delta_{\text{vir}}$ , defined following [Bryan & Norman \(1998\)](#).

[Despali et al. \(2019\)](#) studied the density profile and formation history of these simulated haloes and classified them according to the change in central density from CDM to SIDM. Haloes were classified in two main categories: (i) "CORED" systems, i.e. with lower central density in SIDM with respect to CDM, associated with a low formation redshift and (ii) "CUSPY" system with, conversely, higher formation redshift and higher central density in SIDM. They found that these properties correspond to a difference in the halo mass accretion history and formation redshift: CORED (CUSPY) systems had lower (higher) formation redshift. Among the haloes considered in this work, systems 1-4 belong to the first category (CORED), while the halo 5 to the second (CUSPY). In the left panel of Figure 1, we show the dark matter fraction as a function of radius for the CDM-h (purple triangles) and SIDM-h (blue squares) runs; halo 5 is the only case of a higher central dark matter fraction in SIDM. When

the dark matter fraction is measured in projection (right panel), the differences between the two dark matter models are greatly reduced with respect to the 3D case. Thus, we expect that the effect of baryons on the halo shapes will be especially relevant within  $\approx 30$  kpc from the center.

The zoom-in simulations used in this work reach  $z = 0.2$ , corresponding to the characteristic redshift of the SLACS lenses (Bolton et al. 2006). While this is ideal in the case of a comparison with gravitational lenses (i.e. high redshift galaxies), it might introduce a bias in the comparison to X-ray observations of low- $z$  elliptical galaxies. As shown in Despali et al. (2014), the average halo ellipticity at fixed mass increases with redshift, but it varies by only  $\approx 10$  per cent between  $z = 0$  and  $z = 0.5$ . Throughout this work, we focus on the one-to-one comparison between our simulated samples in different scenarios and thus we think that the effect introduced by SIDM and baryons with respect to CDM would be the same at a different redshift, even if possibly rescaled in magnitude.

### 3 METHODS

The goal of this paper is to quantify the effect SIDM and baryons have on the shapes of ETGs and whether or not CDM and SIDM models with  $\sigma_T/m_\chi = 1 \text{ cm}^2/\text{g}$  can be distinguished on this basis using observations. In this section we introduce our definitions of halo shapes (see also Table 2) and we describe our procedure to create mock X-ray observations from the simulations. Finally, we summarise the observational quantities that we are trying to reproduce and discuss how we compare them to their simulated counterparts, together with the potential limitations. Figures 2 and 3 show examples of the projected dark matter distribution (top panels) and X-ray emission (middle and bottom panels) for one halo and two different projections.

#### 3.1 Halo shapes

Previous works demonstrated that dark matter haloes are well described by triaxial ellipsoids, which approximate the radial matter distribution better than spherical symmetry (Allgood et al. 2006; Despali et al. 2013; Peter et al. 2013; Chua et al. 2019; Despali et al. 2017). Similar to previous works, here we use an iterative method to calculate the halo shapes via the (weighted) inertia tensor, defined as:

$$I_{\alpha\beta} = \frac{1}{N} \sum_{i=1}^N \frac{x_{i,\alpha} x_{i,\beta} m_i}{r_i^2} \bigg/ \sum_{i=1}^N m_i. \quad (1)$$

Here  $\mathbf{x}_i$  are the position components of the  $i$ -th particle from the center of mass,  $\alpha$  and  $\beta$  are the tensor indices,  $m_i$  is the particle mass and  $r_i$  is the distance of the  $i$ -th particle from the center of mass of the halo. We evaluate shapes in shells of increasing radius, with logarithmically-spaced radial bins within  $[0.01, 1] \times R_{\text{vir}}$ . At each radius, we start from a spherical volume and we evaluate the inertia tensor; in order to avoid perturbations due to substructures, we select only the particles belonging to the main halo (i.e. the first subhalo identified by SUBFIND). The squared roots of the three eigenvalues of the inertia tensor define the three axes of the best-fitting ellipsoid at ( $a \geq b \geq c$ ). We define the axis ratios  $s = c/a$  and  $q = b/a$  and the triaxiality parameter  $T = (1 - q^2)/(1 - s^2)$ , that measures how prolate ( $T = 1$ ) or oblate ( $T = 0$ ) the halo is. The eigenvectors determine the spatial orientation of the ellipsoid. We then refine the shape iteratively by deforming the considered region into a triaxial ellipsoid: we use the eigenvectors to rotate the particle distribution and align it with the principal axes, then we select the particles contained in an

ellipsoid enclosing the same volume of the original sphere, using the ellipsoidal distance defined as

$$r_i^2 = dx_i^2/a^2 + dy_i^2/b^2 + dz_i^2/c^2. \quad (2)$$

The inertia tensor is evaluated again on the new set of particles and this procedure is repeated until the axis ratios converge at the one per cent level. At each radius, the shape is calculated independently and the axis ratios and orientation of the ellipsoid are free to vary. In each case, we require a minimum of 1000 particles to guarantee a reliable estimate.

We also measure projected shapes following the same procedure on two projected coordinates: in this case, we calculate the best-fit ellipse, described by two axes ( $a \geq b$ ) and the ellipticity defined as  $e = 1 - b/a$ . As described in more detail in the next Section, we calculate projected shapes along multiple lines of sight: each time, we rotate the halo by randomly choosing three Euler angles ( $\phi, \theta, \psi$ ), where  $\phi$  and  $\psi$  are sampled from a uniform distribution between 0 and  $2\pi$  and  $\theta$  between 0 and  $\pi$ . For each rotated configuration, we then project the mass distribution along the three principal directions and measure the projected shape.

#### 3.2 X-ray maps

We use the pipeline from Barnes et al. (2021) to create X-ray mock images from our CDM-h and SIDM-h simulations, generating the X-ray emission directly from the properties of the gas. We generate mocks corresponding to the properties of *Chandra* and *XMM-Newton* observations, in the soft X-ray energy band 0.5-2 keV.

We begin by generating an X-ray spectrum for every gas particle/cell within the FoF group via a lookup table of spectral templates. We generate the table using the Astrophysical Plasma Emission Code (APEC, Smith et al. 2001). For every particle/cell we compute a total spectrum using its temperature, density and metal abundance by summing over the chemical elements tracked by the simulations, which all track the same elements. The spectrum for every particle is then projected down the relevant axis and smoothed onto a square grid. In each projection, the center of the images is taken to be the projection of the center of the gravitational potential. The pixel size is set to 0.496" arcsec for *Chandra* and 5" for *XMM-Newton*; following common choices from the literature, we convolve the maps with a Gaussian PSF, where the FWHM is assumed to equal the pixel size in both cases. We assume that the mock images do not contain noise or background.

We show examples of the mock images for halo 1, viewed in two different projections in Figure 2 and 3. The middle and bottom panels show the mock X-ray emission as would be observed by *Chandra* and *XMM-Newton* in the soft-bands 0.5-2 keV, from the CDM-h (left) and SIDM-h (right) runs. Comparing the two figures, we can appreciate the effect of looking at the same halo from a different viewing angle: in Figure 2 the CDM-h and SIDM-h cases appear very different, whereas the shapes of the X-ray emission are much closer in Figure 3.

We measure the shapes of the X-ray emission directly from the mock images, following the approach by Buote et al. (2002, see the next Section for more details). In practice, we follow the same procedure that was used for projected shapes, but we weight each pixel (instead of each particle) by its flux (instead of mass) to calculate the inertia tensor. We start by measuring the shapes in circular aperture of increasing radius and, at each radius, the shape of the shell is deformed iteratively into an ellipse with the appropriate orientation and ellipticity. Under the assumption of hydrostatic equilibrium (as

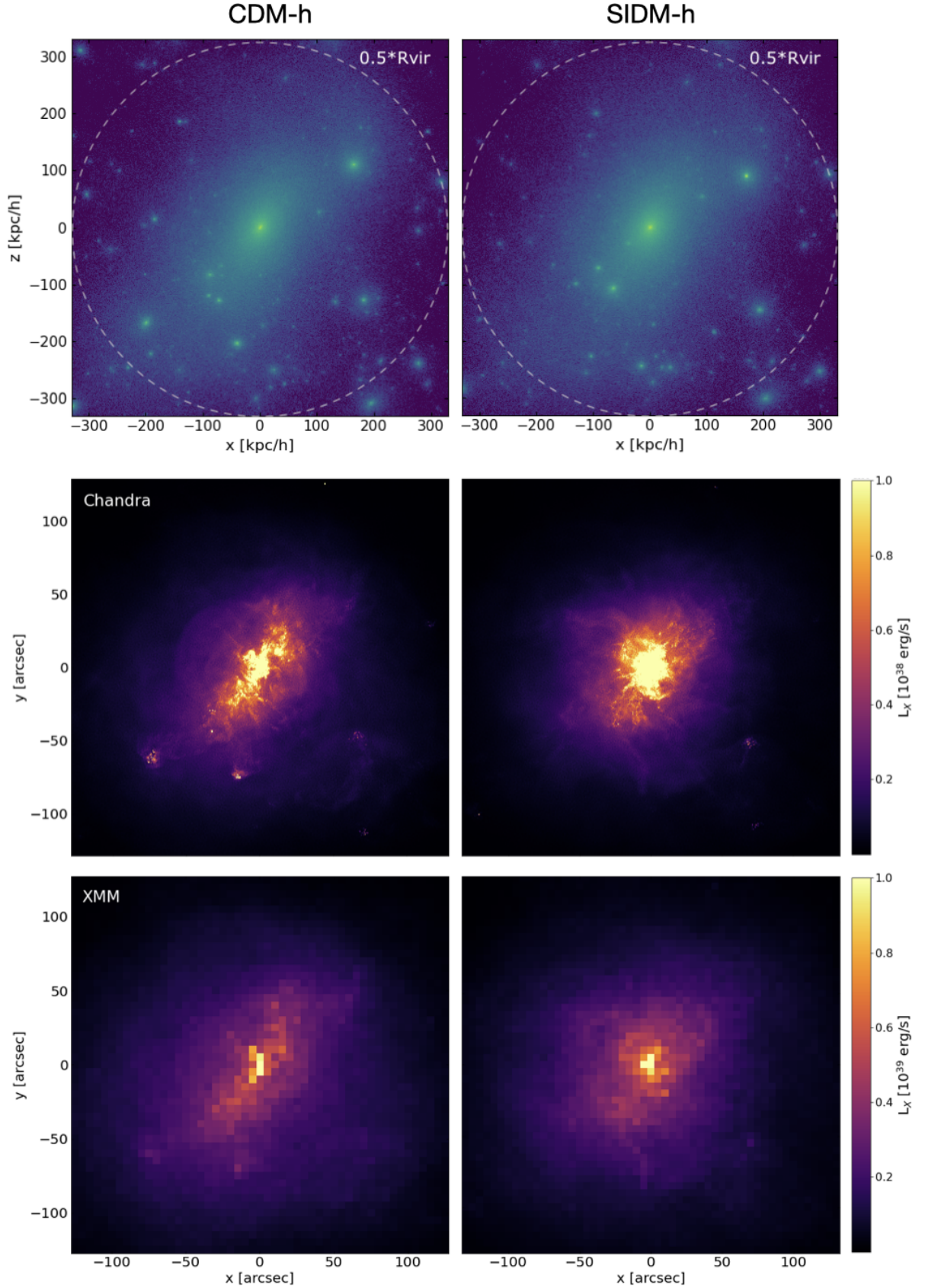


**Figure 2.** Example maps for one system (halo 1) in our sample. The two top panel show the dark matter distribution in the CDM-h and SIDM-h runs. The other four panels show instead the mock X-ray images created using the pipeline described in (Barnes et al. 2021). These are soft band X-ray energies between 0.5 and 2 keV for *Chandra* and *XMM-Newton*, with a resolution of 0.496" and 5" (middle and bottom panels, respectively) and one the same physical scale of the top panels. The images were created with our CDM-h (left) and SIDM-h (right) runs. Note that the Chandra and XMM maps have different limits, respectively in units of  $10^{38}$  and  $10^{39}$  erg/s.

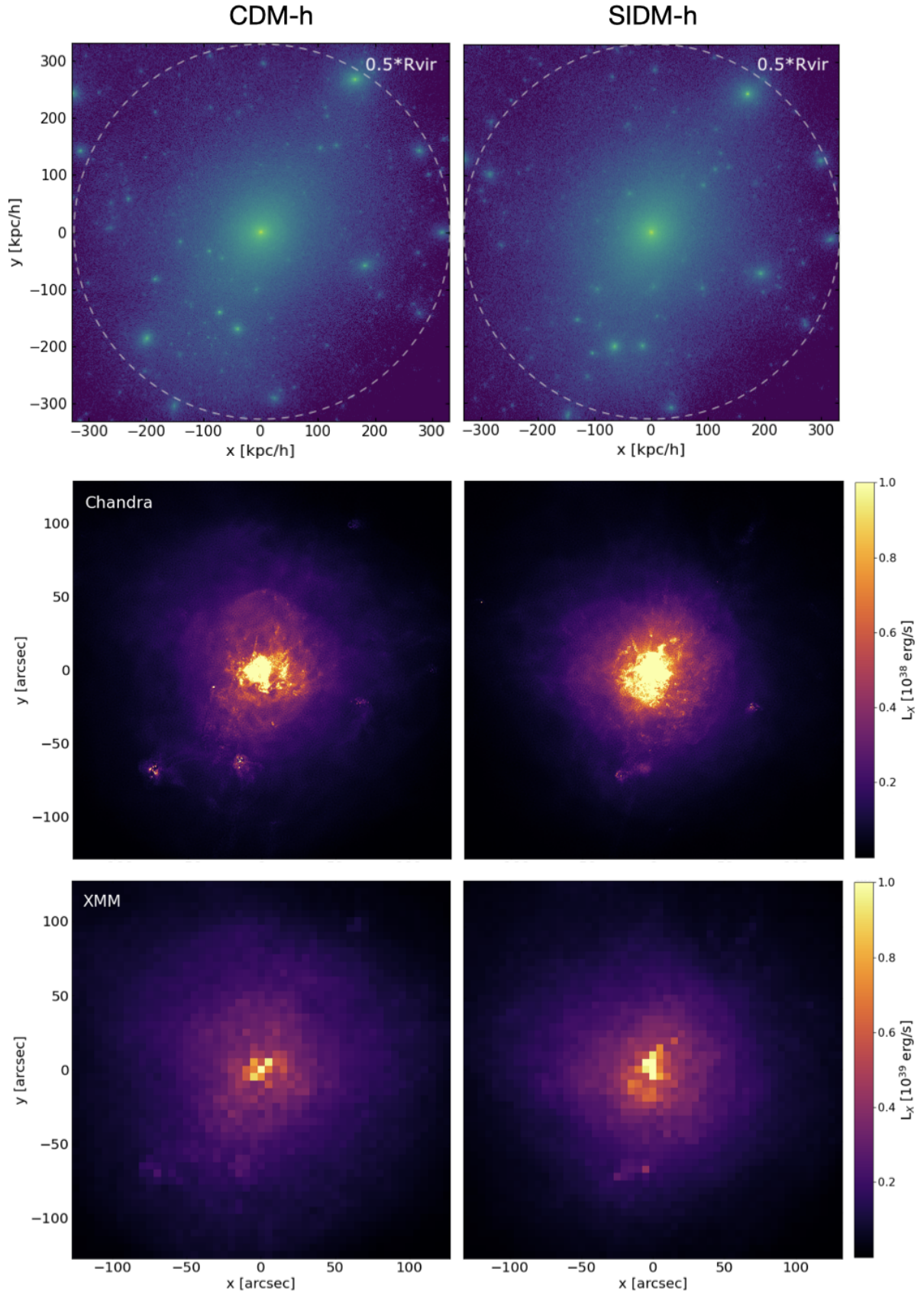


**Figure 3.** Same as Figure 2, but here the same halo is viewed from a different projection.

**Table 2.** Summary of the shape definitions used in this work.

Source	Dimensions	Method	Parameters
simulations	3D triaxial ellipsoid	inertia tensor on mass distribution	axes: $a \geq b \geq c$ axis ratios: $s = c/a$ , $q = b/a$ triaxiality: $T = (1 - q^2)/(1 - s^2)$
simulations	2D projected ellipse	inertia tensor using projected mass	axes: $a \geq b$ ellipticity: $e = 1 - b/a$
simulations	3D spheroid with $a = b$ or $b = c$	inertia tensor on mass distribution	approximation from 3D ellipsoid axes: $a \geq b \geq c$ $\epsilon = 1 - \sqrt{bc}/a$ if prolate $\epsilon = 1 - c/\sqrt{ab}$ if oblate
X-ray observations and mocks	2D	inertia tensor on image pixels	ellipticity $e_X = 1 - b/a$
lensing observations	2D SIE+shear	elongation of the Singular Isothermal Ellipsoid	elongation $q = b/a$ ellipticity $e = 1 - q$

discussed in more details in the next Section), these shapes trace the total gravitational potential of the halo.

### 3.3 Observed quantities

Here we describe the observed quantities that we want to reproduce, previous observational works that we use for comparison with simulations and discuss how they are compared, from the point of view of X-ray observations and gravitational lensing. The shape definitions quoted throughout the paper are summarised in Table 2.

#### X-ray emission

In order to determine the total halo mass through observations of the X-ray emitting gas, one has to rely on the assumption that the gas is in hydrostatic equilibrium and therefore traces the gravitational potential produced by the total mass distribution, a reasonably safe assumption for relaxed elliptical galaxies. Observational works (Buote et al. 2002; McDaniel et al. 2021) measured the shape of the X-ray emission from *Chandra* and *XMM-Newton* observations of elliptical galaxies, by fitting the equivalent of the inertia tensor to the surface brightness distribution in the images. We apply the same technique to the mock images generated from simulations (see Sec 3.2) and derive ellipticity profiles. The results of the comparison are presented and discussed in detail in Section 5.

An alternative approach to compare shapes to numerical predictions is to find the 3D halo shape that best explains the observed ellipticity profile. However, since projected shapes do not probe the elongation along the line-of-sight, it is not possible to directly measure the three-dimensional shape. Previous works describe the halo as an ellipsoid, but only consider the oblate ( $b = c$ ) and prolate ( $b = a$ ) limit configurations that bracket the possible projected ellipticities of a triaxial ellipsoid: in this way, one defines the projected *spheroidal* ellipticity, where the axes are defined in 3D. Peter et al. (2013) converted the triaxial shape measured via the inertia tensor into the *spheroidal* ellipticity in the following way: if the triaxial shape is closer to prolate, then  $\epsilon = 1 - \sqrt{bc}/a$ , while if the shape is closer to oblate  $\epsilon = 1 - c/\sqrt{ab}$ . These choices set the spheroidal volume equal to the ellipsoidal one. In Section 4, we use the same approach and calculate  $\epsilon$  from our simulations and compare to the results by Buote et al. (2002); McDaniel et al. (2021).

#### Gravitational lensing

In strong galaxy-galaxy lensing, the light of a background source is deflected and magnified by the lens galaxy. Bright elliptical/early-type galaxies are the typical lens galaxies. In this context, the entire mass distribution (luminous and dark) contributes to the deflection and can be measured when modelling the lensed images. From the lens modelling, one can reconstruct the two-dimensional lensing potential and the lensing convergence  $\kappa$ , i.e. the Laplacian of the lensing potential. In practice, the convergence is defined as a dimensionless surface density and so effectively corresponds to a scaled projected mass density, characterising the lens system. It can be written as

$$\kappa(x) = \frac{\Sigma(x)}{\Sigma_{\text{crit}}}, \quad \text{with} \quad \Sigma_{\text{crit}} = \frac{c^2}{4\pi G} \frac{D_S}{D_L D_{LS}}, \quad (3)$$

where  $\Sigma_{\text{crit}}$  is the critical surface density and  $D_L$ ,  $D_S$  and  $D_{LS}$  stand respectively for the angular diameter distance of the lens, the source and between the lens and the source. The value of the lensing convergence in practice determines by how much the background sources appear magnified on the lens plane. For non-spherical mass distributions, the lensed images of the source are also stretched and distorted along privileged directions by the shear,  $\gamma$ .

The shape of the lensing convergence should be in practice equivalent to the shape of the total projected mass distribution calculated via the inertia tensor. One important difference lies in the fact that the density profiles of lenses is commonly modeled as a singular isothermal ellipsoid (SIE), with an elongation  $q$ , constant with radius, while we do not include assumptions on the density profile in the shape calculation (but we indeed impose an elliptical shape). However, lensing measurements only probe the mass distribution very close to the galaxy center and thus we do not expect a significant variation of the density profile in this range. Moreover, it has been shown (van de Ven et al. 2009) that for a range of (also non-isothermal) stellar and dark matter density profiles, the isothermal approximation works well around the Einstein radius. A one-to-one comparison would require creating mock lensing images from simulations and model them as real data, which is beyond the scope of this paper and we leave for future work.

In Section 4, we compare our measurements with observational results from two samples of strong gravitational lenses observed with HST: the SLACS (Bolton et al. 2006), the BELLS (Ritondale et al. 2019) and SL2S (Sonnenfeld et al. 2013) lenses, respectively at  $z_l \sim 0.2$ ,  $z_l \sim 0.5$  and  $0.5 \leq z_l \leq 0.8$ . We take the best lens model from previous works (Auger et al. 2010; Ritondale et al. 2019; Sonnenfeld et al. 2013) for a total of 80, 16 and 56 systems, respectively. We

discuss additional technical details of this comparison in Appendix A.

## 4 HALO SHAPES

In this Section, we present the halo shapes calculated directly from the particle distribution in the four considered scenarios. We discuss how the inclusion of self-interactions and baryons influences the 3D and projected shapes and we attempt a first comparison between simulated and observed values.

### 4.1 Triaxial shapes

We start by measuring the intrinsic three-dimensional shape of each halo in our sample. First, we look at the shape of the dark matter component alone in each scenario, to highlight the effect that the presence of baryons has on the underlying distribution of dark matter. The radial profiles of the axis ratios  $s$  and  $q$  and the triaxiality parameter  $T$  are shown in Figure 4, for each halo (columns) and simulation (different colour and associated symbol). At each radius the halo shape is defined by a triaxial ellipsoid, calculated iteratively by deforming the initial spherical volume to find the best match to the mass distribution (see Section 3 for more details). For simplicity, in Figure 4 and in general in all figures in this work, we plot the radial shape profiles as a function of the equivalent spherical radius, i.e. the initial sphere with the same volume of the best-fit ellipsoid at that radius.

We recover the well-known trend in CDM dark-matter-only simulations, where the inner parts of haloes are more elongated (i.e. have smaller axis ratios) than the outskirts (Allgood et al. 2006; Despali et al. 2017; Chua et al. 2019): the inner shape of the halo preserves a trace of the halo merging history and the main direction of accretion, while the outer parts become rounder by subsequent interactions with the field and neighbouring systems. All CDM-d haloes have inner prolate shapes ( $T \rightarrow 1$  and  $s \sim q$ ) and thus, in the approximation by Peter et al. (2013) classify as prolate objects with  $a > b = c$  (see Section 3). This picture is modified both in the presence of self-interactions and baryonic physics, or by the combination of both. In the absence of baryons (SIDM-d runs), the interactions between the dark matter particles modify the central shape and the inner parts of the halo become rounder: the same exchange of energy and momentum that creates the central core also partially erases the central triaxiality and its preferential direction (Peter et al. 2013). This is evident in Figure 4 by comparing the SIDM-d and CDM-d case: with self-interactions, the axis ratios increase towards a spherical case in the inner regions, while the shapes tend to coincide at outer radii.

The inclusion of baryons provides another mechanism to generate shapes that are rounder than in the dark-matter-only case both in CDM-h and SIDM-h haloes. Moreover, the overall trend of shape with radius is reversed and the shapes in the outer parts of the haloes are now more elongated than the center. This can be easily understood by looking at the dark matter fraction as a function of radius (right panel in Figure 1): the baryons dominate in the innermost  $\sim 30$  kpc, while at larger radii dark matter determines the halo properties - where at the same time the lower density makes self-interactions less frequent - and the halo shapes converge to similar values in all models. In CDM-h, our results are compatible with those from previous works (Chua et al. 2019) and in SIDM-h we find an even more pronounced central sphericity, due to the combined effect of baryons and self-interactions (see also Shen et al. 2022; Robertson

et al. 2021). In both cases, and especially in SIDM-h, the haloes move away from a clear prolate shape ( $T = 1$ ) and become more oblate.

We then turn our attention to the baryons and measure the shape of the stellar component that dominates in density at the very center of haloes. We calculate the inertia tensor with the same method that we used for the dark matter and show the results in Figure 5. All our haloes host early-type galaxies in both dark matter scenarios - see the stellar masses in Table 1 and a more detailed description of the galaxy morphologies in Despali et al. (2019). For this reason, we expect these shapes to be quite regular, as the galaxies do not have compact very triaxial components as spiral galaxies. This is indeed the case and the stellar distribution displays a mild and regular trend with radius in all cases. However, it is evident that, not only the halo shape is rounder in SIDM-h, but also the central elliptical galaxy: both axis ratios are on average higher in the SIDM case, supporting the conclusion that the effects self-interactions and baryons push each other in the direction of rounder central shapes.

Finally, we measure the orientation of the best-fit ellipsoid and the misalignment between the dark matter and stellar shapes, in terms of the angle between the major axes. We find misalignments between the two components in agreement with previous works (Velliscig et al. 2015) and that the misalignment is mostly due to the twists of the dark matter distribution as a function of radius - while the stellar distribution maintains an almost constant orientation at all radii (within  $\sim 15$  degrees in both dark matter scenarios).

### 4.2 Projected shapes

In reality, most astrophysical observations cannot measure the three-dimensional shapes of haloes and galaxies, but only projected quantities on the plane of the sky. Given that haloes are triaxial, the projected shape strongly depends on the viewing angle. Thus, to get a statistically relevant measurement, we rotate each halo 30 times and then project the mass distribution along the three principal axes to calculate the projected 2D shape (see Section 3). This results in a sample of  $3 \times 30$  measurements for each halo; we then average together different projections in order to derive a distribution of observed ellipticity.

The results are shown in Figure 6, where we plot the average projected ellipticity  $e = 1 - b/a$  as a function of (the spherical) radius for each system (columns) and simulation (different colors, matching Figure 4). We calculate projected shapes for the dark matter component alone (first row) and for the total mass distribution (second and third row) - these are identical for the CDM-d and SIDM-d runs and differ only in the runs containing baryonic physics. Moreover, we calculate the shapes of the total mass distribution both by considering the enclosed mass at each radius (second row) and the mass in ellipsoidal shells of the same radius (bottom row). For each halo and considered case, we show the mean value of the measured ellipticity together with the  $1\sigma$  region (shaded area). By comparing Figure 6 and Figure 4, we see that - on average - projected shapes are less elongated than triaxial ones and that the projection reduces the differences between different models (Despali et al. 2017). The outer parts of the haloes (that are more similar in all models with respect to the center) that lie close to the center in projection contribute to the shapes. Projection effects also greatly reduce the misalignment between the dark matter and stellar component: we calculate the orientation of the main axes of the best-fit ellipse, by means of the eigenvectors corresponding to the longest axes of both component at each radius, and find that an average misalignment of  $5 \pm 5$  degrees in CDM-h and  $7 \pm 10$  degrees in SIDM-h. For the latter, rounder shapes probably introduce a larger degree of uncertainty in the orientation of the longest axis.

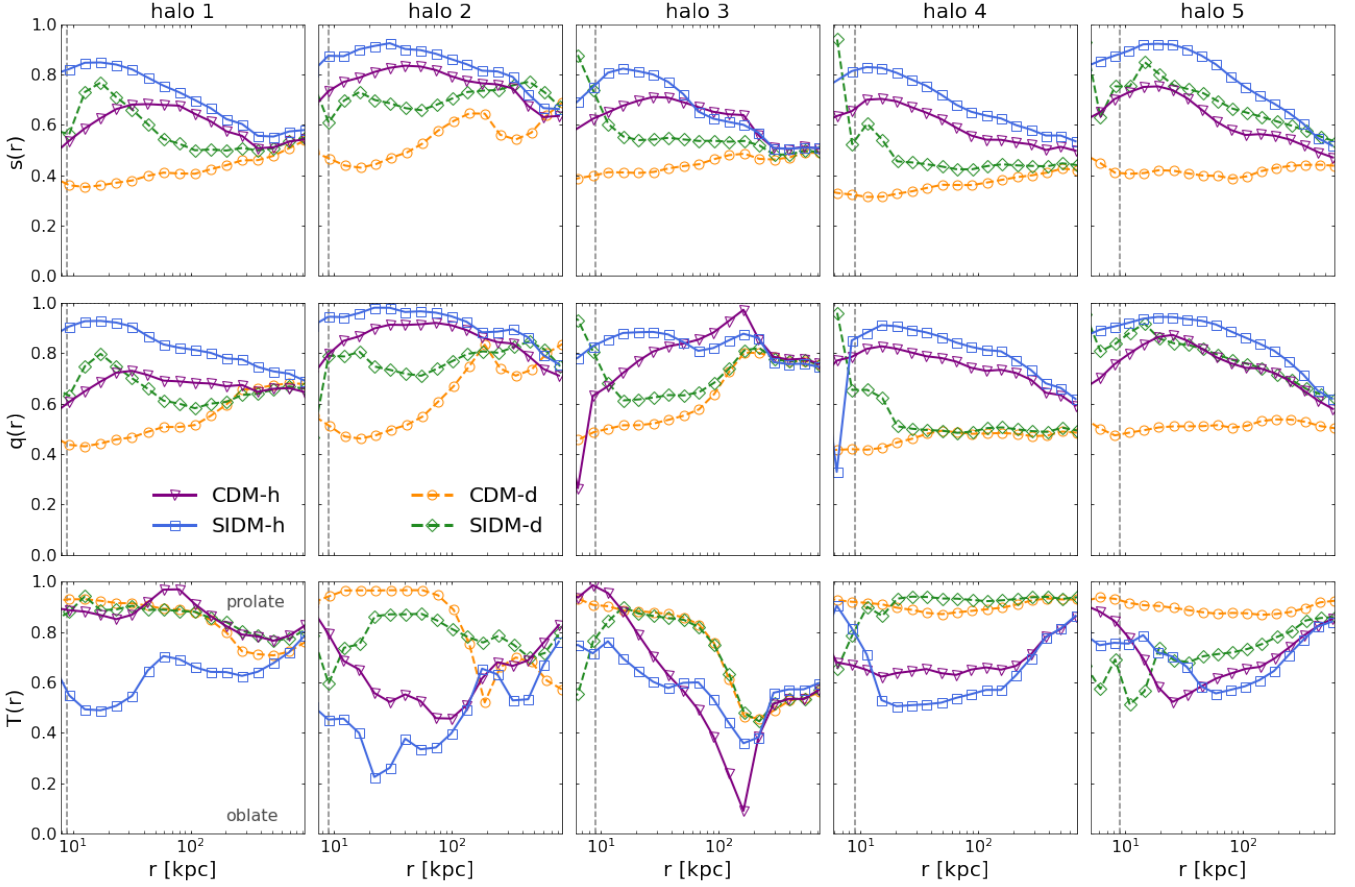


**Figure 4.** Shapes of the dark matter component as a function of (the equivalent spherical) radius in the range  $[0.01, 1] \times R_{\text{vir}}$  for each halo (columns) and simulation; in the top, middle and bottom panels we show the two axial ratios  $s$  and  $q$ , and the triaxiality  $T$ . The CDM-d, SIDM-d, CDM-h and SIDM-h simulations are represented respectively by orange, green, blue and purple lines and circles, diamonds, triangles and squares. We require a minimum of 1000 particles in each bin to calculate the shapes; the vertical dashed line shows the convergence radius calculating for shapes following Chua et al. (2019) and equal to  $9\epsilon$ .

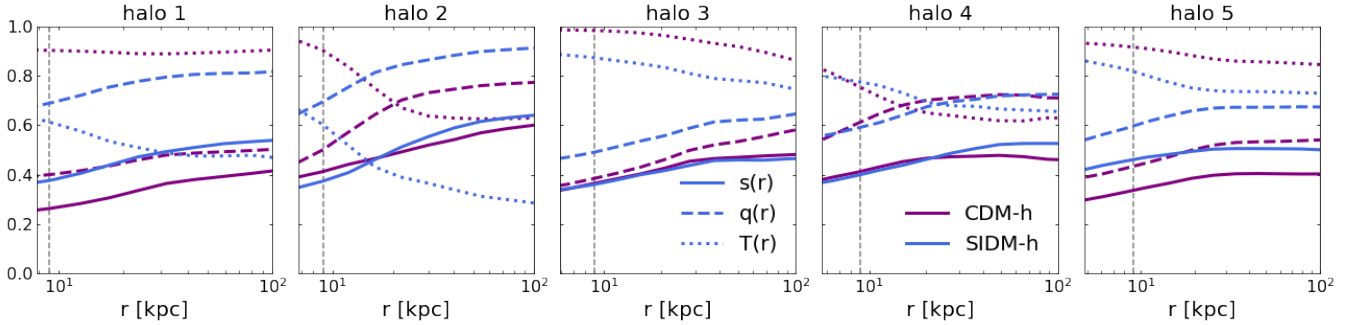


**Figure 5.** 3D shapes of the stellar component in the full physics runs as a function of radius for each halo, in the inner region of the halo between  $0.01 \times R_{\text{vir}}$  and 100 kpc. Solid (dashed, dotted) lines show the axial ratio  $s$  ( $q$ ,  $T$ ) in the CDM-h (purple) and SIDM-h (blue) hydro runs. The vertical dashed line corresponds to the shape convergence radius from Figure 4.

In particular, the SIDM-d shapes have here a very different trend towards the center of the halo where the shape becomes effectively spherical (i.e.  $e=0$ ), while two hydro runs CDM-h and SIDM-h present very similar means for all haloes.

This demonstrates how the inclusion on baryons is thus essential to derive realistic predictions of the observed properties of galaxies and haloes in the real universe, while using dark-matter-only simulations

likely leads to overestimate the differences between CDM and SIDM. A similar effect is found by Robertson et al. (2021) and Mastromarino et al. *in prep* when analysing the halo density profiles of a large number of haloes in SIDM and CDM. In the next Section, we compare the simulated shapes to observed values.

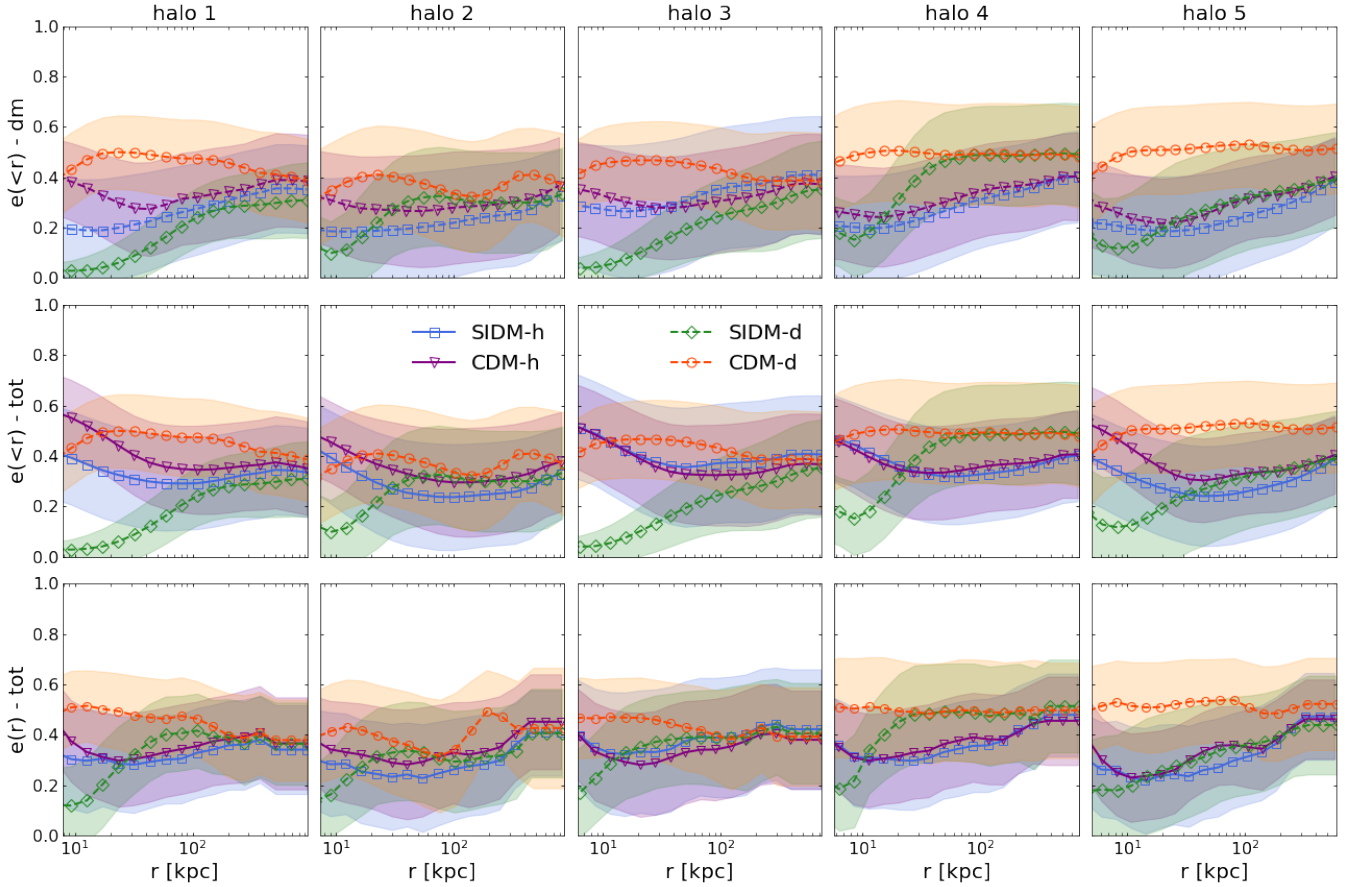


**Figure 6.** Projected shapes. In all panels we show the mean ellipticity profile and associated  $1\sigma$  region (shaded) for each halo (columns) and model (colours and symbols, same as Figure 4). For each halo, we calculated projected shapes in 30 projections and calculate the mean distribution for the projected mass enclosed within an ellipse of radius  $r$  in the top and middle panels - and for the projected mass inside shells of the same radius in the bottom panels. The top panels show the shape of the dark matter component, while the middle and bottom one consider the entire mass distribution. The considered radial range is the same of Figure 4.

### 4.3 Comparison with observational measurements

We now attempt a comparison between the projected ellipticity measured from our runs and observational values coming from: (i) the modelling of gravitational lenses from the SLACS (Auger et al. 2010, 80 lenses), BELLS (Ritondale et al. 2019, 16 lenses) and SL2S (Sonnensfeld et al. 2013, 56 lenses) samples and (ii) the analysis of X-ray emission of elliptical galaxies from Buote et al. (2002, one galaxy) and McDaniel et al. (2021, 11 galaxies), where the projected shape of the potential is recovered by matching the X-ray surface brightness distribution to predictions. See Section 3 for more details. In both cases, we restrict the measurement of projected shapes to the inner part of the haloes in order to compare with observations, choosing the appropriate radii.

In Figure 7 we show the normalised distribution of projected ellipticities  $e$  calculated within  $r = 14$  kpc, that is above the resolution limit and that we choose as an estimate of the area that is probed by lensing. This choice is somewhat arbitrary, given that the SIE profile used for the lens modelling has a constant ellipticity, and comparisons with a different radius could lead to slightly different results. We discuss this aspect in Appendix A. The dashed histograms in the top panel show the results for the dark-matter only runs, while the second and third panel show the ellipticity distribution in the simulations including baryons. The ellipticity distributions differ significantly in

the dark-matter-only runs, reproducing previous results (Peter et al. 2013). However, when it comes to the runs including baryons the two distributions are significantly closer, especially when the total mass distribution is considered (third row) instead of the dark matter component alone (second row). We note, however, that the SIDM-h distribution presents a higher tail at very low ellipticities  $e \simeq 0$ , that is not present in the CDM-h case: its presence (or absence) could be used to distinguish between the two models, instead of focusing only on the mean values.

Finally, the bottom panel summarises the ellipticity distribution from observational works: the solid, dashed and dotted histograms reports the projected ellipticity from the three considered samples. We can already see by eye that none of them are compatible with the distribution predicted by the CDM-d dark matter-only case (orange histogram), whereas they look close to the hydro results. As mentioned in Section 3, we have not gone through the process of creating mock images from the simulations and modelling them as real data, which we leave for future work, and thus the comparison could be biased. However, we impose an elliptical shape that can adapt to the mass distribution in terms of orientation and ellipticity (similar to the SIE used in observations) and we use only the particles belonging to the main halo - this should reduce the need of accounting for a

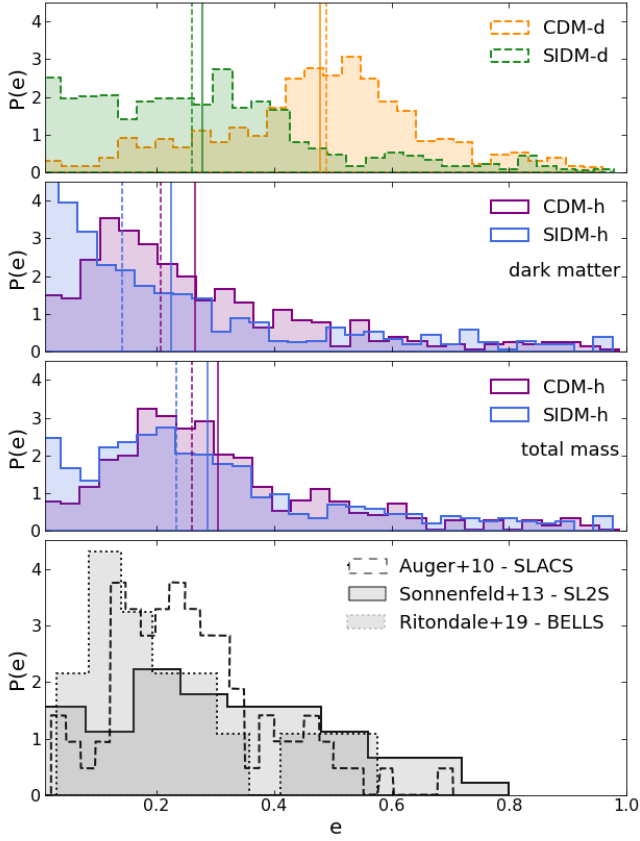


**Figure 7.** Distribution of projected ellipticity at the center of the haloes. For simulated values (first three rows), we plot the ellipticity at a distance from the halo center within  $r = 14$  kpc. The top panel shows the distributions derived from the dark-matter-only runs, whereas for the hydro runs, we show the results calculate both by using the dark matter particles only (second row) and dark matter plus baryons together (third row). In each panel, the vertical solid (dashed) lines of corresponding color show the mean (median) of each distribution. Finally in the bottom panel, we report the observational distributions derived from gravitational lenses in the SLACS (Auger et al. 2010), BELLS (Ritondale et al. 2019) and SL2S (Sonnenfeld et al. 2013) samples.

possible source of shear in our simulated data. We refer to Appendix A for more details.

We use the Kolmogorov-Smirnov (KS) test to quantitatively compare the simulated and observed lensing samples: we test their compatibility against the null hypothesis that they are sampled from the same parent distribution. The tables in Figure 8 report the results of the test for each combination of samples, in terms of the KS distance and  $p$ -value. The former is in practice the maximum distance between the cumulative distribution functions of the two samples, while the latter is the probability of observing this maximum difference under the assumption that the parent distribution is the same. If the KS statistic is small or the  $p$ -value is high, then we cannot reject the null hypothesis in favor of the alternative.

First, we compare the simulated samples with each other (left panels of Figure 8): in all cases the  $p$ -value is small, indicating that it is possible to distinguish between the simulated samples. The stronger differences are between the CDM-d and SIDM-d runs and between the CDM-h and CDM-d runs - in this case we are sure that they cannot be drawn from the same parent distribution, and vice versa.

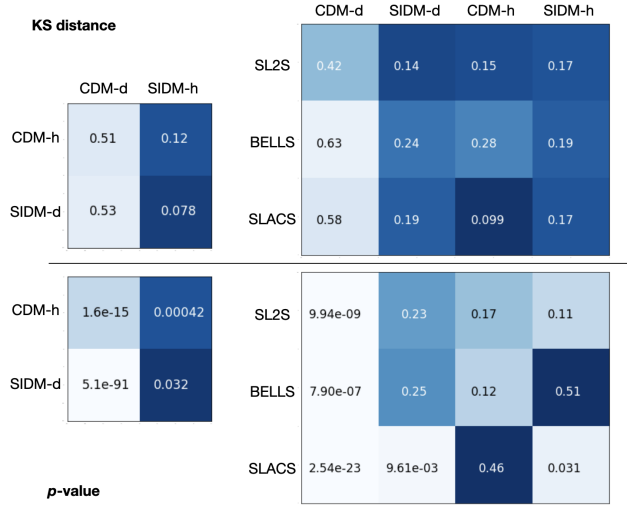


**Figure 8.** Results of the KS test for each pair of data-sets. In the left panel, we compare the simulated distributions to each other and show the KS distance (top) and the corresponding  $p$ -value (bottom). Similarly, in the right panels, we compare the simulated samples with observations and show again the KS statistics (top) and the  $p$ -values (bottom). When the KS distance is large and/or the  $p$ -value is small (light blue), two samples are unlikely to be drawn from the same parent distribution. In the cases presented here, the more compatible pairs are thus those corresponding to darker shades of blue.

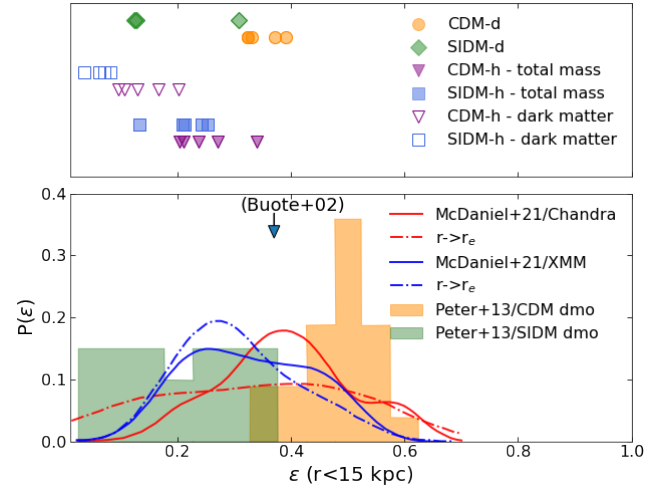


**Figure 9.** Distribution of *spheroidal* ellipticity parameter  $\epsilon$  at a distance from the halo center  $r < 15$  kpc. Since this is a measure of the 3D shape, we only have five values (one per halo) per model, shown in the top panel. These are calculated from the triaxial axes as described in Section 3 and following Peter et al. (2013). In the bottom panel, we report the observational distributions from McDaniel et al. (2021) for *Chandra* and *XMM-Newton* data and the result from Buote et al. (2002) on NGC 720, as well as the distributions from the dark-matter-only simulations from Peter et al. (2013).

In the right panels, we show instead the comparison between simulated and observed lens samples. All observational distributions clearly disfavour the high ellipticities from the CDM-d run, with high KS values and extremely low  $p$ -values (first column). The BELLS sample clearly favours the SIDM-h case and the SLACS lenses the CDM-h run, clearly rejecting the two dark runs. The SL2S lenses show a slightly higher preference for the SIDM-d distribution, how-

ever not much higher than CDM-h. The other combinations are less likely, but cannot be fully ruled out and, in general, the degree of preference for each sample could be due to the different technique used to obtain observed and simulated values. What is evident is that the data reject the CDM-d predictions and require the presence of a component that can increase the central sphericity in order to explain the distribution of observed shapes. Moreover, the CDM and SIDM hydro runs produce very similar predictions and are difficult to distinguish with the current amount of observational measurements, or from a different point of view, both models could explain the data. This means that previous constraints on the self-interaction cross-section  $\sigma$  might overestimate our ability to distinguish between these two models only by looking at the shapes. The comparison done here is based on the shapes measured within  $r = 14$  kpc: in Appendix A, we show the KS and  $p$ -values trends with radius and we demonstrate that the overall trends are valid even for a different choice of radius up to 40 kpc from the center, while discussing other possible sources of bias.

Finally, we compare the projected shapes with results from X-ray studies. In the next Section, we expand this comparison by analysing mock X-ray images. We remind the reader that the definition of ellipticities shown so far differ slightly from those reported by Buote et al. (2002) and Peter et al. (2013), because we plot the projected ellipticities  $e$  and not the *spheroidal* ellipticities  $\epsilon$  (see Section 3); given our small sample of haloes, we cannot obtain a full distribution of the latter, but only one value per halo. However, we calculate the  $\epsilon$  value (see Section 3) of each halo at  $r < 15$  kpc (consistently with the observational analysis from previous works) and show a comparison in Figure 9. In practice, all our haloes are prolate in the inner parts and thus we use the three axes of the best-fitting ellipsoid to calculate  $\epsilon = 1 - \sqrt{bc}/a$ , corresponding to the points in the top panel. In the bottom panel, the dashed and solid curves report the observational results from McDaniel et al. (2021), who calculated the distribution of *spheroidal* ellipticity of haloes that would better reproduce the observed ellipticity profiles. For comparison the coloured histograms show the results from dark-matter-only simulations from Peter et al. (2013), who used the same method to calculate  $\epsilon$  from the 3D shapes. Unfortunately in this case, we cannot draw significant conclusions, as our statistics are limited; we will discuss a more meaningful comparison with this data set in the next Section, where we analyse the shape profiles and not limit the comparison to a specific radius.

## 5 SHAPES OF X-RAY IMAGES

We use the pipeline from (Barnes et al. 2021) to create mock X-ray luminosity maps, as described in Section 3 and shown in Figure 2 and 3. We generate 90 maps for each halo by rotating the particle distribution, similarly to the case of projected 2D shapes. In this case, we use the total gas distribution in the halo (and not only that belonging to the main subhalo), for a more realistic comparison with real X-ray images that may contain luminous satellites.

We measure the ellipticity of the X-ray emission in each map by calculating the inertia tensor directly on the image, following Buote et al. (2002); McDaniel et al. (2021). As described in Section 3, we use an approach analogous to the measurements of projected shapes in simulations, but using the pixels and fluxes instead of the particle positions and masses. We measure the shapes in shells of increasing radius, where the initial circular aperture is deformed iteratively into an ellipse in order to match the surface brightness distribution. We then calculate the mean ellipticity for the CDM-h and SIDM-h cases. Figure 10 shows the X-ray ellipticity  $e_X(r)$  in the *Chandra* (left) and

*XMM-Newton* (right) mock images. Thin purple (blue) lines show the results for each halo in the CDM-h (SIDM-h) scenarios, whereas the thick lines of corresponding colour stand for the mean, together with the associated standard deviation. At the very center, the CDM-h shapes are more elongated (but still compatible within the shaded regions), but this effect quickly disappears at distances  $r \geq 25$  kpc and the ellipticity profile becomes flat. Our results are consistent with the cluster-scale measurements from Shen et al. (2022), who also found a maximum mean difference of  $\approx 0.1$  in the central ellipticity (in their case, within  $0.1 \times R_{vir}$ ) which then disappears further away from the halo center. *XMM-Newton* shapes are rounder than the corresponding *Chandra* measurements, due to the lower resolution that smooths out part of the elongation.

In the bottom panels, we compare - at each radius - the ellipticities  $e_X$  with those obtained in Section 4 by modelling the projected mass distribution (see Figure 6). The mean ellipticities inferred from the X-ray mock images are lower than those measured from the projected mass distribution. This is consistent with the fact that the gas - under the hypothesis of hydrostatic equilibrium - traces the gravitational potential, which is rounder than the mass distribution by construction (Golse & Kneib 2002). We show one visual example of these differences in Figure 11.

Apart from this difference, the X-ray ellipticities in CDM-h and SIDM-h are even closer to each other than the values calculated from the projected mass difference: it seems unlikely that we will be able to distinguish between the two dark matter scenarios only by measuring the shape of the X-ray emitting gas. However, it is encouraging that the simulated images are a good representation of real observations: in Figure 12 we compare the mean ellipticity profiles to the observational profiles measured by McDaniel et al. (2021) for nine galaxies, using *Chandra* and *XMM-Newton* data in the same band. We only use the systems for which they report observations with both instruments. Despite the object-to-object variation and the difference in redshift between simulations and observations, the overall trend is well reproduced by the *Chandra* mocks. In the case of *XMM-Newton*, some observed systems display an increase of ellipticity at  $r > 30$  kpc that we do not see so strongly in our simulations. However, given the small sizes of both samples, we cannot judge whether this is a real discrepancy or an effect of the limited statistics.

Based on this comparison, we cannot discard one of the two dark matter scenarios, nor establish if one of the two should be preferred: both the CDM model and a SIDM model with constant cross-section of  $\sigma_T/m_X = 1 \text{ cm}^2/\text{g}$  are consistent with the data.

Finally, we note that an important difference between the observational analysis and the simulated mock images is that we have assumed that the latter are noise-free and that the background is irrelevant, while this is obviously not the case for observational data.

## 6 SUMMARY AND DISCUSSION

Using zoom-in re-simulations of a sample of massive galaxies at  $z = 0.2$  (see Despali et al. 2019), we investigate the possibility of discriminating between CDM and a self-interacting dark matter model with constant cross-section  $\sigma/m = 1 \text{ cm}^2/\text{g}$  on the basis of halo shapes. To this end, we measure the three-dimensional and projected shapes of the dark matter and total mass distribution of five systems, simulated in the two considered scenarios, with (CDM-h and SIDM-h) or without (CDM-d and SIDM-d) the inclusion of baryonic physics - thus a total of four runs per halo. Our main results are:

- we recover the well-known trend in CDM dark-matter-only sim-

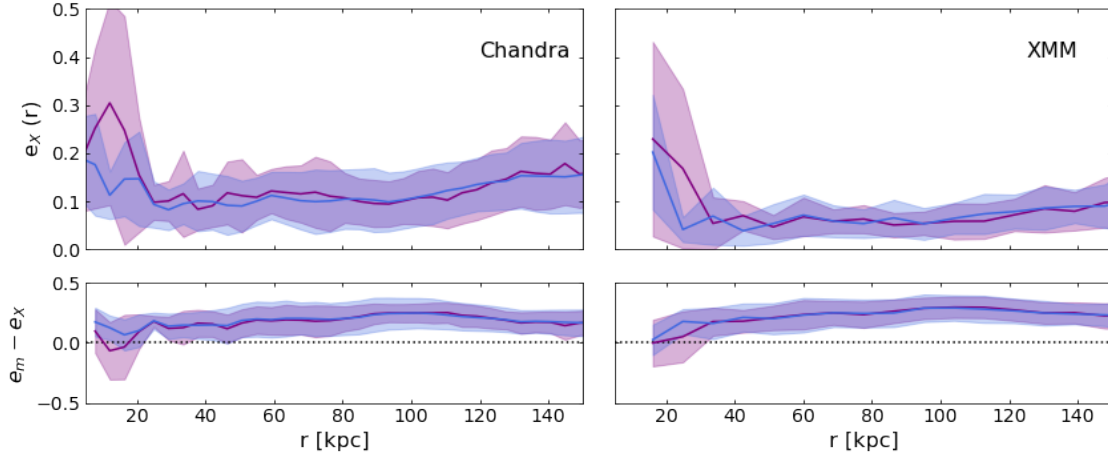


**Figure 10.** Shapes of the X-ray emission, measured in ellipsoidal shells by calculating the inertia tensor of the mock images, created to match *Chandra* (left) and *XMM-Newton* (right) observations. The solid lines and the shaded area stand for the mean and standard deviation of the ellipticity profile  $e_x$  as a function of radius. In the bottom panel, we show the mean difference between the ellipticity calculated from the projected mass density in Section 4 and that of the X-ray emission. The first describes the mass distribution, while the second traces the gravitational potential and is rounder by construction.

ulations, where the inner parts of the haloes are more elongated than the outskirts;

- similarly, we reproduce the results of previous works on SIDM dark-matter-only simulations, where the self-interactions in the high-density center of the halo produce rounder shapes;
- we find that the inclusion of baryons on average leads to rounder shapes both in the CDM and SIDM scenarios and that the predictions from the two dark matter models are very similar when hydrodynamical simulations are used;
- the effect of both baryons and self-interactions influences the shape of the inner part of the halo, while for each halo the shapes converge to the same values at large radii in all scenarios: far from the centre the dark matter dominates the density, but at the same time the density is low and thus self-interactions are less frequent than in the center;
- we measure projected shapes along 90 random viewing angles for each system and calculate the ellipticity of the projected mass distribution: the mean projected shapes are closer to spherical and more difficult to distinguish compared to the three-dimensional measurements, due to the contribution of the outer part of the haloes that fall into the considered projected radius.

We then compare the distribution of simulated shapes to observational results in the context of gravitational lensing (Auger et al. 2010; Sonnenfeld et al. 2013; Ritondale et al. 2019) and X-ray (Buote et al. 2002; McDaniel et al. 2021) studies. In the case of gravitational lensing, we compare the projected shapes - measured in the simulations from the mass density distribution within 14 kpc - to the ellipticity of the best SIE profile that was measured from the lensing convergence. We use three lens samples: the SLACS (Bolton et al. 2006; Auger et al. 2010), the BELLS (Ritondale et al. 2019) and the SL2S (Sonnenfeld et al. 2013) lenses. The average redshift of the samples is  $z = 0.2$  for the SLACS (corresponding to the final snapshot of our simulations that is used for the measurements),  $z = 0.5$  for the BELLS and  $z = 0.3$  for the SL2S. While we do not expect a significant variation of the mean halo shapes in this range in redshift, this could in principle introduce a bias in the comparison.

We perform a Kolmogorov-Smirnov test to determine whether or not the observed samples are drawn from the same distribution of one of the simulations. We find that

- all the lens samples strongly reject the CDM-d model, which produces too high elongations;
- the SLACS (BELLS) sample prefers the simulated results from the CDM-h (SIDM-h) run. However, none of the samples clearly rejects the other simulated results (from CDM-h, SIDM-h and SIDM-d);
- these trends are valid for most radii in the range between 5 and 30 kpc and the CDM-h (followed by SIDM-h) provides the best overall match at all radii (see Appendix A);
- when applied to the simulated values only, the KS test is able to distinguish between the samples.

Finally, we create mock X-ray maps from the simulations including baryonic physics, using the method described in Barnes et al. (2021). We simulate *Chandra* and *XMM-Newton* observations in the soft X-ray energies between 0.5 and 2 keV, by rotating each halo along different viewing angle, as done with the projected mass distribution. We measure the shapes directly from the imaging, by applying the same procedure used to evaluate the inertia tensor on the image pixels and fluxes (Buote et al. 2002; McDaniel et al. 2021). Under the assumption of hydrostatic equilibrium, the X-ray emission describes the gas distribution and thus directly traces the gravitational potential of the halo. We analysed the ellipticity profiles and compared them with those of observed elliptical galaxies from McDaniel et al. (2021), in the same band and at similar resolution. We find that:

- the ellipticity profiles  $e_x$  are flat at large radii ( $r > 25$  kpc), with an average ellipticity of  $\approx 0.15$ ;
- towards the center, the X-ray ellipticity increases and CDM-h shapes can be larger than SIDM-h ones by a factor of two, but still compatible within  $1\sigma$ ;
- the X-ray ellipticities are smaller ( $\sim$ half) than those calculated from the projected mass distribution at the same radius, as expected by the fact that the gravitational potential is rounder than the mass distribution;
- the ellipticity profiles are compatible with the *Chandra* and *XMM-Newton* observational results from McDaniel et al. (2021) both for the CDM-h and SIDM-h scenarios.

We conclude that both CDM and a SIDM model with constant cross-section  $\sigma/m_\chi = 1\text{cm}^2/\text{g}$  are compatible with the most recent

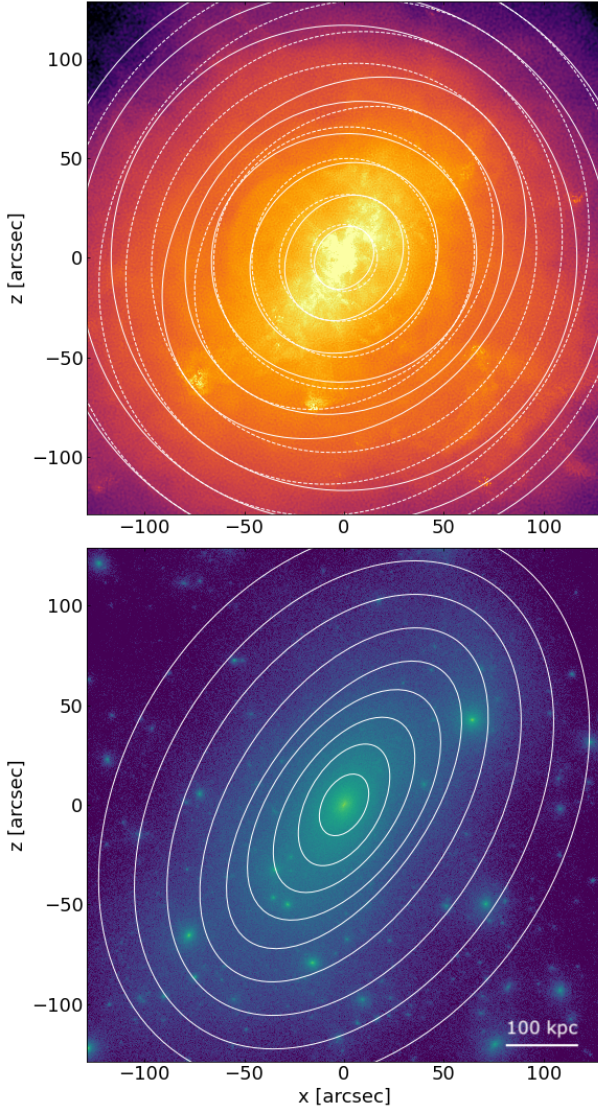


**Figure 11.** Halo shapes from the X-ray emission vs. projected mass distribution. In the top panel we show the *Chandra* simulated emission for a projection of halo 1 (see Figure 2, together with the best-fit elliptical shells estimated by measuring the inertia tensor of the image (solid white line). The dashed lines show instead the ellipticity estimated from the corresponding *XMM-Newton* mock image, at the same radii. In the bottom panel, we show instead the projected dark matter density, together with the elliptical shells that best fit the projected mass distribution. These more elongated than the ones in the top panel, as predicted by the difference between the shape of the mass and the potential. They have, however, similar orientation.

observations of elliptical galaxies. This is consistent with the conclusions by [McDaniel et al. \(2021\)](#), whereas other previous works based on the comparison to dark-matter-only simulations ([Buote et al. 2002](#); [Peter et al. 2013](#)) found a preference for SIDM models with  $\sigma_T/m_\chi \approx 0.1 \text{ cm}^2/\text{g}$  and disfavoured higher cross-section like the one used in this work. It is evident how the inclusion of baryons in the simulated results is of fundamental importance to derive realistic predictions. In general, larger samples of simulations as well as of observations will help us to derive more precise predictions. Moreover, methods that can decompose the mass distribution into dark matter and baryonic components separately might give a better chance of distinguish CDM and SIDM models.

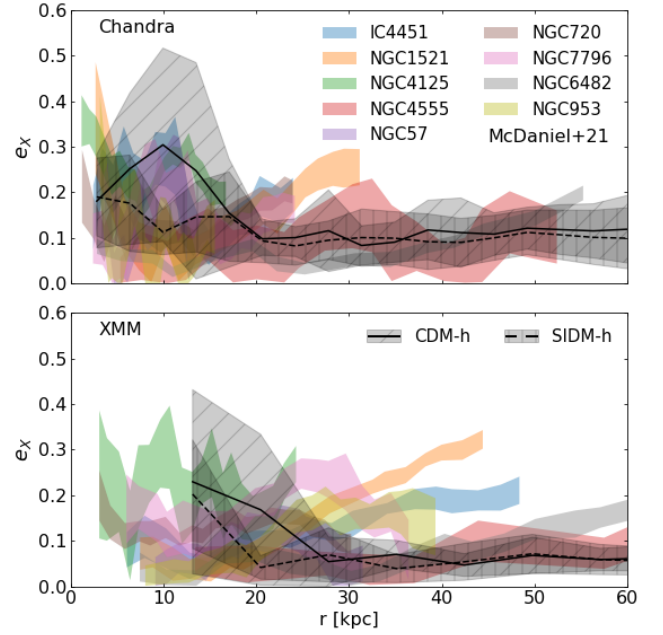


**Figure 12.** Comparison between the mean ellipticity profiles derived from the CDM-h (solid line) and SIDM-h (dashed line) runs and the measurements for nine elliptical galaxies from [McDaniel et al. \(2021\)](#), shown by bands of different colours.

Here, we have used "classic" SIDM simulations with elastic scattering and constant cross-section, but many other SIDM models are still viable alternatives to CDM, such as models with velocity-dependent cross section ([Zavala et al. 2019](#); [Robertson et al. 2021](#)), inelastic scattering ([Vogelsberger et al. 2019](#)) or more complex models including dark radiation ([Vogelsberger et al. 2016](#)). It is also worth mentioning that the CDM-h and SIDM-h hydro runs have been created without re-calibrating the baryonic physics model - both contain the standard TNG model ([Pillepich et al. 2018](#)). Having run only a sample of zoom-in simulations, we do not know if all the standard galaxy scaling relations would be reproduced in a SIDM cosmological box and if using the same hydro model forces a similarity between the SIDM-h and CDM-h halo shapes. However, this would require a much larger computational effort and our results represent a first step forward towards more realistic predictions.

Our results can be interpreted both in a pessimistic and optimistic light. On one hand, it is less straightforward than previously estimated to discriminate between the two considered models by measuring at the shapes of galaxies and their haloes. On the other hand, both models can well reproduce observed distribution and thus are both viable explanations for the properties of elliptical galaxies, leaving us with alternatives in case one of the two models is challenged by other observations or at a different mass scale.

## ACKNOWLEDGMENTS

We are grateful to the IllustrisTNG collaboration for allowing the use of the IllustrisTNG model for [Despali et al. \(2019\)](#), on which this work is based. We thank David Barnes for sharing his X-ray pipeline with us. GD thanks Luca Di Mascolo for useful discussion about X-ray data and Ralf Klessen for his thorough comments on the paper draft. MS acknowledges support by the European Research Council under ERC-CoG grant CRAGSMAN-646955. JZ acknowledges

support by a Grant of Excellence from the Icelandic Research fund (grant number 206930). SV acknowledges funding from the European Research Council (ERC) under the European Union's Horizon 2020 research and innovation programme (LEDA: grant agreement No 758853).

## DATA AVAILABILITY

The simulations as well as the codes to analyze them will be made available upon request to the corresponding author. This research made use of the public python packages Astropy (Astropy Collaboration et al. 2013), matplotlib (Hunter 2007), NumPy (Harris et al. 2020) and SciPy (Jones et al. 01 ).

## REFERENCES

- Allgood B., Flores R. A., Primack J. R., Kravtsov A. V., Wechsler R. H., Faltenbacher A., Bullock J. S., 2006, *MNRAS*, **367**, 1781
- Andrade K. E., Fuson J., Gad-Nasr S., Kong D., Minor Q., Roberts M. G., Kaplinghat M., 2022, *MNRAS*, **510**, 54
- Astropy Collaboration et al., 2013, *A&A*, **558**, A33
- Auger M. W., Treu T., Bolton A. S., Gavazzi R., Koopmans L. V. E., Marshall P. J., Moustakas L. A., Burles S., 2010, *ApJ*, **724**, 511
- Barnes D. J., Vogelsberger M., Pearce F. A., Pop A.-R., Kannan R., Cao K., Kay S. T., Hernquist L., 2021, *Monthly Notices of the Royal Astronomical Society*
- Benítez-Llambay A., Frenk C. S., Ludlow A. D., Navarro J. F., 2019, *MNRAS*, **488**, 2387
- Blumenthal G. R., Faber S. M., Flores R., Primack J. R., 1986, *ApJ*, **301**, 27
- Bolton A. S., Burles S., Koopmans L. V. E., Treu T., Moustakas L. A., 2006, *ApJ*, **638**, 703
- Brinckmann T., Zavala J., Rapetti D., Hansen S. H., Vogelsberger M., 2018, *MNRAS*, **474**, 746
- Bryan G. L., Norman M. L., 1998, *ApJ*, **495**, 80
- Bullock J. S., Boylan-Kolchin M., 2017, *ARA&A*, **55**, 343
- Buote D. A., Jeltema T. E., Canizares C. R., Garmire G. P., 2002, *ApJ*, **577**, 183
- Burger J. D., Zavala J., 2021, *ApJ*, **921**, 126
- Chua K. T. E., Pillepich A., Vogelsberger M., Hernquist L., 2019, *MNRAS*, **484**, 476
- Chua K. T. E., Dibert K., Vogelsberger M., Zavala J., 2021, *MNRAS*, **500**, 1531
- Colín P., Avila-Reese V., Valenzuela O., Firmani C., 2002, *ApJ*, **581**, 777
- Davé R., Spergel D. N., Steinhardt P. J., Wandelt B. D., 2001, *ApJ*, **547**, 574
- Despali G., Vegetti S., 2017, *Monthly Notices of the Royal Astronomical Society*, 469, 1997
- Despali G., Tormen G., Sheth R. K., 2013, *Monthly Notices of the Royal Astronomical Society*, 431, 1143
- Despali G., Giocoli C., Tormen G., 2014, *MNRAS*, **443**, 3208
- Despali G., Giocoli C., Bonamigo M., Limousin M., Tormen G., 2017, *MNRAS*, **466**, 181
- Despali G., Sparre M., Vegetti S., Vogelsberger M., Zavala J., Marinacci F., 2019, *Monthly Notices of the Royal Astronomical Society*, 484, 4563
- Enzi W., Vegetti S., Despali G., Hsueh J.-W., Metcalf R. B., 2020, *MNRAS*, **496**, 1718
- Garrison-Kimmel S., et al., 2019, *MNRAS*, **487**, 1380
- Genel S., et al., 2014, *MNRAS*, **445**, 175
- Gnedin O. Y., Kravtsov A. V., Klypin A. A., Nagai D., 2004, *ApJ*, **616**, 16
- Golse G., Kneib J. P., 2002, *A&A*, **390**, 821
- Harris C. R., et al., 2020, *Nature*, 585, 357
- Hunter J. D., 2007, *Computing In Science & Engineering*, 9, 90
- Jones E., Oliphant T., Peterson P., et al., 2001–, SciPy: Open source scientific tools for Python, <http://www.scipy.org/>
- Kaplinghat M., Tulin S., Yu H.-B., 2014, *Phys. Rev. D*, **89**, 035009
- Kaplinghat M., Valli M., Yu H.-B., 2019, *MNRAS*, **490**, 231
- Kaplinghat M., Ren T., Yu H.-B., 2020, *J. Cosmology Astropart. Phys.*, **2020**, 027
- Kim S. Y., Peter A. H. G., Hargis J. R., 2018, *Phys. Rev. Lett.*, **121**, 211302
- Lovell M. R., Zavala J., Vogelsberger M., 2019, *MNRAS*, **485**, 5474
- Mashchenko S., Couchman H. M. P., Wadsley J., 2006, *Nature*, **442**, 539
- McDaniel A., Jeltema T., Profumo S., 2021, *J. Cosmology Astropart. Phys.*, **2021**, 020
- Miralda-Escudé J., 2002, *ApJ*, **564**, 60
- Navarro J. F., Frenk C. S., White S. D. M., 1997, *ApJ*, **490**, 493
- Oñorbe J., Boylan-Kolchin M., Bullock J. S., Hopkins P. F., Kereš D., Faucher-Giguère C.-A., Quataert E., Murray N., 2015, *MNRAS*, **454**, 2092
- Pakmor R., Springel V., 2013, *MNRAS*, **432**, 176
- Peter A. H. G., Rocha M., Bullock J. S., Kaplinghat M., 2013, *Monthly Notices of the Royal Astronomical Society*, 430, 105
- Pillepich A., et al., 2018, *MNRAS*, **473**, 4077
- Pontzen A., Governato F., 2012, *MNRAS*, **421**, 3464
- Read J. I., Agertz O., Collins M. L. M., 2016, *MNRAS*, **459**, 2573
- Ritondale E., Auger M. W., Vegetti S., McKean J. P., 2019, *MNRAS*, **482**, 4744
- Robertson A., et al., 2018, *MNRAS*, **476**, L20
- Robertson A., Massey R., Eke V., Schaye J., Theuns T., 2021, *MNRAS*, **501**, 4610
- Rocha M., Peter A. H. G., Bullock J. S., Kaplinghat M., Garrison-Kimmel S., Oñorbe J., Moustakas L. A., 2013, *MNRAS*, **430**, 81
- Roszkowski L., Sessolo E. M., Trojanowski S., 2018, *Reports on Progress in Physics*, **81**, 066201
- Sameie O., Creasey P., Yu H.-B., Sales L. V., Vogelsberger M., Zavala J., 2018, *MNRAS*, **479**, 359
- Sameie O., Yu H.-B., Sales L. V., Vogelsberger M., Zavala J., 2020, *Phys. Rev. Lett.*, **124**, 141102
- Schaller M., et al., 2015, *MNRAS*, **451**, 1247
- Schaye J., Crain R. A., Bower R. G., Furlong M., Schaller M., Theuns T., Dalla Vecchia C., Frenk C. S. e. a., 2015, *MNRAS*, **446**, 521
- Shen X., Brinckmann T., Rapetti D., Vogelsberger M., Mantz A., Zavala J., Allen S. W., 2022, arXiv e-prints, [p. arXiv:2202.00038](https://arxiv.org/abs/2202.00038)
- Smith R. K., Brickhouse N. S., Liedahl D. A., Raymond J. C., 2001, *ApJ*, **556**, L91
- Sonnenfeld A., Gavazzi R., Suyu S. H., Treu T., Marshall P. J., 2013, *ApJ*, **777**, 97
- Sparre M., Springel V., 2016, *MNRAS*, **462**, 2418
- Sparre M., Pfrommer C., Ehlert K., 2020, *MNRAS*, **499**, 4261
- Springel V., et al., 2005, *Nature*, **435**, 629
- Tollet E., et al., 2016, *MNRAS*, **456**, 3542
- Torrey P., Vogelsberger M., Genel S., Sijacki D., Springel V., Hernquist L., 2014, *MNRAS*, **438**, 1985
- Tulin S., Yu H.-B., 2018, *Phys. Rep.*, **730**, 1
- Velliscig M., et al., 2015, *MNRAS*, **453**, 721
- Verde L., Treu T., Riess A. G., 2019, *Nature Astronomy*, **3**, 891
- Vogelsberger M., Zavala J., Loeb A., 2012, *MNRAS*, **423**, 3740
- Vogelsberger M., et al., 2014a, *MNRAS*, **444**, 1518
- Vogelsberger M., Zavala J., Simpson C., Jenkins A., 2014b, *MNRAS*, **444**, 3684
- Vogelsberger M., Zavala J., Cyr-Racine F.-Y., Pfrommer C., Bringmann T., Sigurdson K., 2016, *MNRAS*, **460**, 1399
- Vogelsberger M., Zavala J., Schutz K., Slatyer T. R., 2018, preprint, ([arXiv:1805.03203](https://arxiv.org/abs/1805.03203))
- Vogelsberger M., Zavala J., Schutz K., Slatyer T. R., 2019, *MNRAS*, **484**, 5437
- Vogelsberger M., Marinacci F., Torrey P., Puchwein E., 2020, *Nature Reviews Physics*, **2**, 42
- Weinberger R., et al., 2017, *MNRAS*, **465**, 3291
- Zavala J., Lovell M. R., Vogelsberger M., Burger J. D., 2019, *Phys. Rev. D*, **100**, 063007
- Zolotov A., et al., 2012, *ApJ*, **761**, 71
- van de Ven G., Mandelbaum R., Keeton C. R., 2009, *MNRAS*, **398**, 607

**APPENDIX A: COMPARISON WITH LENSING DATA AT DIFFERENT RADII**

In Section 4, we compared the projected ellipticities measured from simulations to the results of gravitational lensing observations. In Figure 7 and 8, we have chosen the projected ellipticities measured within  $r = 14$  kpc from the center, where this distance was chosen as an approximate estimate of the size of the region probed by lensing. However, not all observed lenses have the same angular or physical size and thus the comparison could be biased by this specific choice. Moreover, the observational modelling includes an external shear component that we do not have in the simulation analysis. On the other hand, here we calculate the shapes only on the projected mass distribution of the main halo (i.e. the first SUBFIND subhalo) and discard the subhalo contribution (and do not have any external source of possible shear) and thus we expect it to trace an ellipticity similar to that of the SIE.

Here, we repeat the KS-test for different projected distances between 5 and  $30 \text{ kpc} h^{-1}$  from the center: for each radius, we compare the simulated shapes to the observational results (these do not change). The results are shown in Figure A1: in each column, we plot the  $p$ -value (top) and KS distance (bottom) for the comparison between one simulated data-set and the three considered lensing samples.

It is evident that the CDM-d predictions are strongly rejected in all cases, confirming the results from Figure 8. Moreover, the SIDM-d predictions are compatible with the observational data only in the range between 10 and  $20 \text{ kpc} h^{-1}$ , whereas inner and outer shapes are disfavoured. Finally, the CDM-h predictions seem to provide the best agreement with observational data, followed closely by SIDM-h results. This test confirms the main conclusion drawn in Section 4: thanks to the addition of baryons, both cold and self-interacting dark matter are viable explanations for observed shapes.

This paper has been typeset from a  $\text{\LaTeX}$  file prepared by the author.

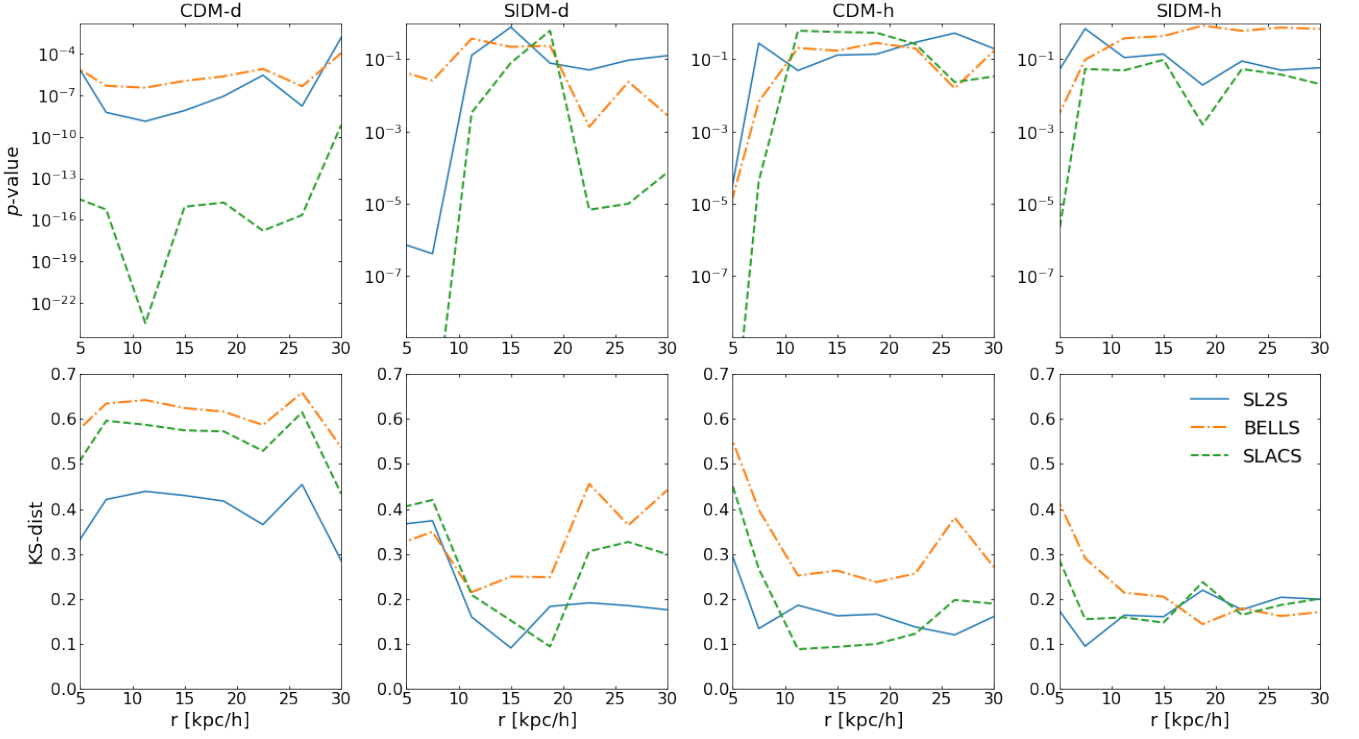


**Figure A1.** We show how the KS distance (bottom) and the associated  $p$ -value (top) of the comparison between simulations and observational data depend on radius. Lines of different colours show the results for the SL2S (Sonnenfeld et al. 2013), BELLS (Ritondale et al. 2019) and SLACS (Auger et al. 2010) observed ellipticity, when compared with the simulated values (different columns). Note that the y-axis does not have the same limits in all panels in the top row. We remind the reader that if the KS-distance is low and the  $p$ -value is high, two samples are likely to be drawn from the same distribution. Conversely, if the KS-distance is high and/or the  $p$ -value is low (as in the leftmost panels), it is unlikely that two samples are drawn from the same parent distribution.